Atomic Force Microscopy Breaking Through the Vertical Range-Bandwidth Tradeoff

Shingo Ito, Mathias Poik,
Johannes Schlarp, and Georg Schitter, *Senior Membership*

Abstract—This paper proposes a mechatronic system design for atomic force microscopes (AFMs) in order to realize a large range and high control bandwidth of the vertical probe motion by a flexure-guided voice coil actuator. The first mechanical resonant frequency of the actuator is decreased to 67 Hz for a large motion while the second resonant frequency is maximized to 1.15 kHz. The frequency band between the resonances enables two-degree-of-freedom control with a position sensor to realize a control bandwidth of 881 Hz, which is 13 times higher than the first resonance that is the limitation of conventional AFMs. The closed-loop actuator achieves a positioning resolution of 1.7 nm and a nonlinearity of 0.02 % for a motion range of 700 μm. Consequently, the actuator realizes a range-bandwidth product of 617 kHz·μm, breaking through a theoretical limit of piezoelectric actuators (567 kHz·μm). The high performance of the actuator is further confirmed by 400 μm topography measurement in the constant force mode with a bandwidth of 197 Hz. The achieved resolution of the topography measurement is 2.9 nm, and it is demonstrated by successfully imaging nanostructures on a CD-ROM disk.

Index Terms—Atomic force microscopy, Mechatronics, Nanopositioning, Precision engineering, Design for control.

I. INTRODUCTION

ATOMIC force microscopes (AFMs) are equipped with a sharp probe moved by high-precision actuators [1], [2]. Their application has been extending since the invention [3], including instrumentation, imaging, and nanomachining [4]. For example, AFMs repair photomasks [5] and measure nanostructures on ICs for quality control [6] in the semiconductor manufacturing industry. For inline metrology [7] (e.g. of coating [8] and grinding [9]) topography measurement with nanometer resolution is desired in the production lines directly. For such industrial applications outside the laboratory environments, a large vertical motion of the AFM probe is desired not only for high topography measurement, but also for the sample height uncertainties (e.g. thermal expansion during AFM operation). However, the range and the control bandwidth of the probe's vertical motion are restricted for imaging in a tradeoff, which is influenced by the vertical actuator types.

Piezoelectric actuators

Piezoelectric actuators are most commonly used as the vertical actuator in AFMs and realize extremely high control bandwidths [10], [11]. It is typically limited by the first dominant resonant frequency ω_1 [12], which is usually the natural frequency $\sqrt{k/m_m}$ given with the mover mass m_m and the actuator stiffness k [13]. Thus, the high intrinsic stiffness of the piezoelectric materials is ideal for large k and consequently for high control bandwidth, which may be further increased by flexures. In return, however, the increased stiffness k reduces the achievable motion range z_{max} for a given force to approximately 10 μm or less [14]. This results in a design tradeoff to determine k between the achievable bandwidth and range.

For piezoelectric actuators, a theoretical limit of the tradeoff has been derived by using a stack actuator model without an end mass (payload) [15], [16], which is approximated by

$$\omega_c z_{max} \leq \omega_1 z_{max} \leq 10^{-3}\sqrt{3v_m},\tag{1}$$

where ω_c and v_m are the control bandwidth and the speed of sound in the piezoelectric material [17], respectively. The upper bound of $\omega_1 z_{max}$ is about 300-400 kHz·μm [11] or 567 kHz·μm theoretically [16]. In reality, both off-the-shelf and custom-made piezo-actuated systems have a trend to take a significantly smaller value, due to the end mass that decreases the first resonant frequency (see [16]).

Electromagnetic actuators

For a large motion and linearity, flexure-guided Lorentz (voice coil) actuators are selected as the vertical actuator of AFMs (see Table II) although their stray flux may be a concern for certain AFM modes (e.g. magnetic force microscopy). Lorentz actuators utilize the Lorentz force that is independent of the mover position within a uniform magnetic field (i.e. zero-stiffness property) [13]. Thus, the flexures dominate the actuator stiffness k, which is decreased by their design for a large motion range [6], [14], [18]. However, soft flexures decrease ω_1 and restricts the bandwidth of the probe's deflection control [19] due to the mechatronic system design (see Sec. III-A and Sec. V-A). This results in a range-bandwidth tradeoff in the same manner as the piezoelectric actuators. In fact, ω_1 can be increased to more than 100 kHz by a tiny electromagnetic actuator less than a few millimeters while the achievable range is less than a micrometer [20].

Although the tradeoff may be overcome by a mechanism without flexures such as magnetic levitation or air bearing [21], [22], its mover is heavy and bulky. This is because such mechanisms require multiple actuators or gravity compensation with a pneumatic counter balance [22] or permanent magnets [21], [23]. A heavy mover restricts the achievable acceleration and speed [13], and a bulky mover can create mechanical resonances and antiresonances at relatively low frequencies. Overall, the performance of compact AFMs are restricted by the range-bandwidth tradeoff of the probe's vertical motion, which is problematic to further improve the throughput and workspace of AFM systems.

This paper proposes a mechatronic system design for an AFM with a flexure-guided Lorentz actuator for the probe's vertical motion. The mechanical design takes account of not only the first resonance ω_1, but also the second resonance ω_2 analytically. The flexures are designed so that ω_2 is sufficiently higher than ω_1. Such a design enables to eliminate the model uncertainty between ω_1 and ω_2 and to compensate for the first resonance by feedback control with a position sensor. Consequently, the flexure-guided Lorentz actuator achieves a control bandwidth ω_c that is far higher than ω_1, overcoming the range-bandwidth trade-off. In other words, the flexures are designed by considering the effect of control in advance to maximize the closed-loop system performance. This design concept is regarded as Design For Control (DFC) [24], and its effectiveness is experimentally investigated.

The paper is organized as follows. Section II describes an AFM that integrates the proposed design, and Section III presents its flexure design for DFC. The AFM's dynamics are identified in Section IV for the position control design to compensate for the first resonance in Section V. Section VI presents the deflection control of the probe for the AFM experiments in Section VII, followed by the discussion in Section VIII and the conclusion in Section IX.

II. SYSTEM ARCHITECTURE

A laboratory setup that integrates the proposed design is shown in Fig. 1, where a mover is suspended by flexures along the vertical Z axis. The mover is vertically moved by a compact Lorentz actuator (AVM20, Akribis, Singapore), which is driven by a custom-made current amplifier with a bandwidth of 24 kHz. The resistance, the inductance, and the maximum current of the Lorentz actuator are 0.50 mH, 3.59 Ω, and 0.78 A$_{\text{rms}}$, respectively. For AFM imaging as a demonstration, the backside of the mover mounts a self-sensing AFM probe (PRS-L70-F900-Si-PCB, SCL-Sensortech, Vienna, Austria), which has a resonant frequency at 0.5-1.3 MHz. A sample is placed on a manual Z stage with a micrometer and laterally scanned by an XY scanner (NPXY100-100, nPoint, Middleton, USA). To compensate for dynamics of the suspended mover including the suspension mode at the natural frequency, an interferometer (IDS3010, attocube, Haar, Germany) is installed as a position sensor that measures the distance between the mover and the stator.

A lumped-parameter model of the proposed AFM is shown in Fig. 2(a), where the counter force of the AFM probe is
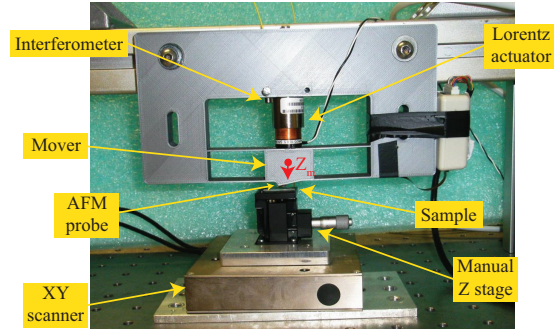

Fig. 1. Photograph of an AFM that integrates the proposed design.

neglected because the force between the probe and the sample is usually sufficiently small to protect the probe. The equation of motion about the mover is

$$F = m_m \ddot{z}_m + c\dot{z}_m + kz_m, \qquad (2)$$

where m_m and z_m are the mass and the vertical position of the mover, respectively, and c and k denote the damping and the stiffness of the flexures, respectively. The Lorentz actuator generates the force F given by

$$F = K_m I, \qquad (3)$$

with the motor constant $K_m = 2$ N/A and the coil current I. Notice that F is independent of z_m, which is the zero-stiffness property of Lorentz actuators. This property may also be realized by another type of actuators (e.g. flux-controlled hybrid reluctance actuator [25]). Since the interferometer measures the mover position, its output y_m equals to z_m. The AFM probe detects the probe deflection, which is proportional to the mover-sample distance, and its output y_p is given by

$$y_p = k_p(z_m - z_s), \qquad (4)$$

where z_s and k_p are the sample position including the topography to be imaged and the probe sensitivity with its preamplifier, respectively. Because I is proportional to the current amplifier's reference V_r, the Laplace transform of the above equations gives a transfer function from V_r to y_m, which is arranged as follows [26]:

$$P(s) = g_p \left(\frac{s^2}{\omega_1^2} + 2\zeta \frac{s}{\omega_1} + 1 \right)^{-1}, \qquad (5)$$

using

$$g_p = \frac{g_a K_m}{k}, \qquad \zeta = \frac{c}{2\sqrt{km_m}}, \qquad \omega_1 = \sqrt{\frac{k}{m_m}}, \qquad (6)$$

where g_a, g_p, ζ, and ω_1 are the amplifier gain (0.2 A/V), the plant gain, the damping ratio, and the first resonant frequency due to the suspension mode, respectively.

In practice, the transfer function from V_r to y_m additionally includes a phase lag (e.g. due to the sampling) and parasitic mechanical modes. They can be modeled by augmenting $P(s)$ as follows

$$P_a(s) = y_m(s)/V_r(s) = P_{pl}(s)(P(s) + P_{hm}(s)). \qquad (7)$$

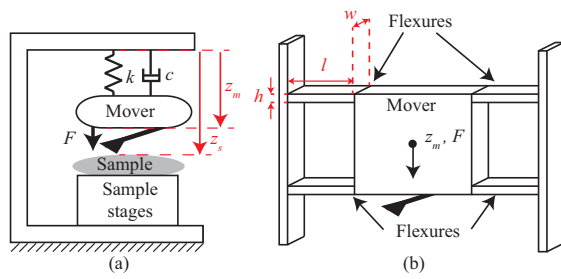IEEE TRANSACTIONS ON INDUSTRIAL ELECTRONICS

Fig. 2. Models of the proposed AFM: (a) lumped-parameter model and (b) leaf-spring flexures.
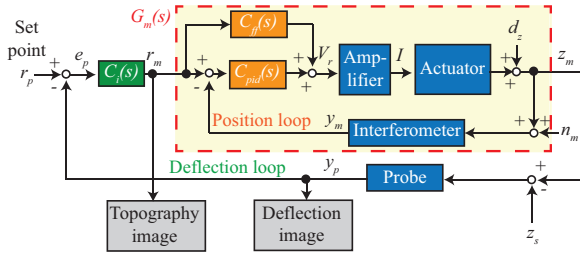

Fig. 3. Control architecture of the proposed AFM.

The transfer functions $P_{pl}(s)$ and $P_{hm}(s)$ model the phase lag and the parasitic mechanical modes, respectively, and are given by [27]

$$P_{pl}(s) = \frac{1 - \frac{\tau}{2}s}{1 + \frac{\tau}{2}s}, \quad P_{hm}(s) = \sum_{i=2}^{N_m} \frac{R_{m,i}}{s^2 + 2\zeta_i \omega_i s + \omega_i^2}, \quad (8)$$

where τ and N_m are the delay and the number of the mechanical modes, respectively. The residue, the damping ratio, and the eigenfrequency of the i-th mode are denoted by $R_{m,i}$, ζ_i, and ω_i, respectively.

The above modeling is visualized in Fig. 3, together with the control architecture of the proposed AFM. In the same manner as conventional AFMs, the proposed AFM controls the deflection of the probe by the deflection loop, which is important for high topography measurement without damaging the sample (i.e. constant force mode [1]). The problem of conventional AFMs is that the bandwidth of the deflection control is limited by the first resonant frequency, as discussed in Sec. I. To compensate for the actuator's dynamics including the corresponding suspension mode, the proposed AFM uses cascade control including the internal position loop with the position sensor (Fig. 3). The cascade control is implemented by a prototyping control system (DS1005, dSpace GmbH, Paderborn, Germany) with a sampling frequency of 20 kHz. The following sections present the detailed design and analysis of the flexures and the control.

III. FLEXURE DESIGN FOR CONTROL

A. System design concept

Although the internal position loop in Fig. 3 itself was proposed for the vertical motion control of an AFM probe,

the bandwidth could not exceed the first resonant frequency [28]. One of the challenges of typical vertical actuators is that the first resonance is close to the higher resonances that are denoted by $P_{hm}(s)$ in the frequency domain, and they are usually difficult to model accurately. The resulting model uncertainty of $P_{hm}(s)$ near ω_1 restricts the achievable control bandwidth below ω_1 [19], [28].

In the proposed AFM design, a flexure-guided Lorentz actuator is selected because the resonant frequencies are determined by the flexure design due to the zero-stiffness property unlike piezoelectric actuators. In the flexure design, ω_1 is deceased for a large motion range while the second dominant resonant frequency ω_2 is maximized, such that the uncertainty of $P_{hm}(s)$ occurs at high frequencies. This mechanical design creates a smooth -40 dB/dec line beyond ω_1 in a Bode plot (see Fig. 4). The dynamics decrease the uncertainty between ω_1 and ω_2 without dominant resonances and anti-resonances. Such dynamics enable the position loop to realize a control bandwidth that is significantly higher than ω_1, as well as high linearity and high robustness.

B. Motion range and required force

Among different types of flexures, compound flexures are often used for a large motion [29]. They require ancillary movers that can create new mechanical modes at low frequencies to limit the control bandwidth [30]. Therefore, leaf spring flexures are selected without ancillary movers, as shown in Fig. 2(b), where l, w, and h are the length, the width, and the height of the flexures.

The flexure dimensions are related to the flexure stiffness k by calculating the bending moment [31], as follows:

$$k = nEwh^3/l^3, \quad (9)$$

where E and $n = 4$ are the Young's modulus and the number of the flexures, respectively. The stiffness k relates the maximum motion range $z_{max,dc}$ at a steady state and the required force

$$F_{req} = kz_{max,dc}, \quad (10)$$

where $z_{max,dc}$ is set to 250 μm for a sufficient range. Notice that the actuator is bidirectional, and the maximum stroke of the actuator is 500 μm, which is larger than conventional AFMs by a factor of about 50.

C. Resonant frequencies

The first resonant frequency in (2) is given by [13]

$$\omega_1 = \sqrt{k/m_m}, \quad (11)$$

under an assumption that the mover is rigid and sufficiently heavier than the flexures with sufficiently small c. By applying this assumption to a distributed-parameter model of the leaf spring flexures, the second resonant frequency ω_2 along the Z axis is analytically given [31] and arranged as follows:

$$\omega_2 = \gamma\omega_1\sqrt{m_m/m_f} = \gamma\sqrt{k/m_f}, \quad (12)$$

where $\gamma = 6.45$ is a constant, and the flexure mass m_f is given by $nwhl\rho$ with the material density ρ. The above equation

IEEE TRANSACTIONS ON INDUSTRIAL ELECTRONICS

TABLE I
FLEXURE DESIGN PARAMETERS AND VALUES GIVEN BY (9)-(12).

| Symbol	Value	Unit	Symbol	Value	Unit
E	3.15	GPa	ρ	1240	kg/m^3
l	35	mm	w	17	mm
h	0.8	mm	$z_{max,dc}$	250	μm
m_m	24.7	g	m_f	2.36	g
ω_1	51.3	Hz	ω_2	1.07	kHz
ω_2/ω_1	20.8	-	F_{req}	0.64	N

Fig. 4. Measured Bode plot from the current amplifier's reference V_r to the interferometer output y_m, which the plant model $P_{pl}(s)P(s)$ is fit to.

clearly gives the flexure design guideline that m_f needs to be minimized with respect to m_m, in order to maximize the gap between ω_1 and ω_2 in the frequency domain [31].

Eq. (12) additionally reveals that ω_2 is independent of the mover mass m_m, unlike ω_1 in (11). This fact gives the design freedom to broaden the ω_2/ω_1 frequency band, which is utilized to overcome the range-bandwidth tradeoff of the vertical motion in the proposed AFM.

D. Flexure design and fabrication

For compact monolithic design and quick manufacturing, the flexures are made together with the mover and the stator by a 3-D printer (i3 MK3, Prusa, Praha, Czech Republic) based on fused deposition modeling (FDM) [32]. Commonly used polylactic acid (PLA) filaments [33] selected as the material determine the parameters ρ and E. For simplicity, the mover is designed as a cuboid, providing a sufficient space to mount the Lorentz actuator and the AFM probe.

The design parameters h, l, and w in (9) are tuned to maximize ω_2 in (12) for a high control bandwidth under the constraint that F_{req} is less than 50 % of the maximum actuation force (1.56 N$_{rms}$). This ensures a sufficient margin for the tolerance of FDM [34]. Table I lists the used and obtained parameter values. The force constraint results in a small k and ω_1 for a large motion. In other words, the flexure design widens the frequency band between ω_1 and ω_2, and Table I predicts that it is more than a decade ($\omega_2/\omega_1 = 20.8$). In the next section, the predicted values are experimentally evaluated.

IV. SYSTEM IDENTIFICATION

To validate the flexure design, a Bode plot of the assembled system is measured from the current amplifier's reference V_r to the interferometer output y_m, and the plant model $P(s)$ in (5) is fit by tuning its parameters, as shown in Fig. 4. The values identified by the fitting are $g_p = 40.4$ dB, $\zeta = 0.0714$, and $\omega_1 = 66.7$ Hz at first. As the second step, the phase lag is captured for analysis by setting the delay τ to 75 μs as indicated by $P_{pl}(s)P(s)$ in Fig. 4. The parasitic modes are not captured by $P_{hm}(s)$ for demonstration that the proposed design overcomes the bandwidth-range tradeoff even without an accurate model of $P_{hm}(s)$.

The second dominant mode ω_2, which influences the closed-loop stability (see Sec. V-A), is 1.15 kHz in Fig. 4. The measured ω_1 and ω_2 are 30 % and 7.5 % higher than the
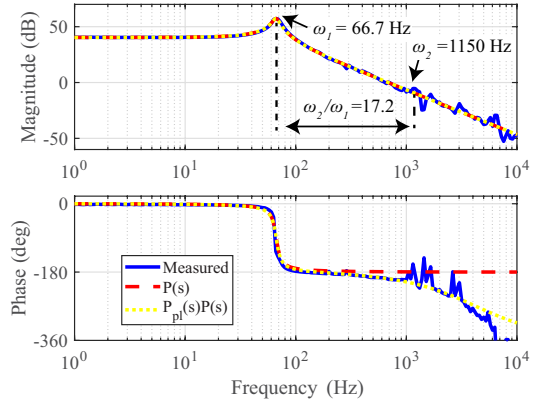
analytically predicted values in Table I. The mismatch would be due to the manufacturing error and the material properties influenced by the manufacturing process [34]. Overall, by considering both ω_1 and ω_2 in the flexure design, a wide frequency band of $\omega_2/\omega_1 = 17.2$ has been successfully realized in Fig. 4, as intended in the design. As a result, a -40 dB/dec line is visible between ω_1 and ω_2.

V. POSITION CONTROL

This section presents the position control of the mover by using a two-degree-of-freedom (2-DOF) controller that consists of a feedback controller $C_{pid}(s)$ and feedforward controller $C_{ff}(s)$, as shown in Fig. 3.

A. Feedback control

To compensate for the first resonance by $C_{pid}(s)$, the open-loop cross-over frequency $\omega_{o,pid}$ must be higher than ω_1. Because the phase is about -180° between ω_1 and ω_2 in Fig. 4, $C_{pid}(s)$ needs to provide a phase lead around $\omega_{o,pid}$ for closed-loop stability. This means that certain controllers (e.g. I and PI) are unsuitable to increase $\omega_{o,pid}$ beyond ω_1. In this article, a PID controller with a low pass filter is configured to provide a sufficient phase lead beyond ω_1 [35] as follows:

$$C_{pid}(s) = g_{pid}\left(1 + \frac{\omega_{z,pid}}{s}\right)\left(\frac{3s + \omega_{o,pid}}{s + 3\omega_{o,pid}}\right), \quad (13)$$

where g_{pid} and $\omega_{z,pid}$ are a gain and a corner frequency. Based on a simulation with the measured response in Fig. 4, the other parameters are tuned to maximize $\omega_{o,pid}$, satisfying phase margin (PM) and gain margin (GM) [13], [36] of more than 30° and 6 dB, respectively. The tuned parameters are $\omega_{o,pid} = 500$ Hz, $\omega_{z,pid} = 50$ Hz, and $g_{pid} = -5.71$ dB. The corresponding open-loop transfer function is shown in Fig. 5, indicating sufficient PM and GM of 33° and 7.7 dB, respectively.
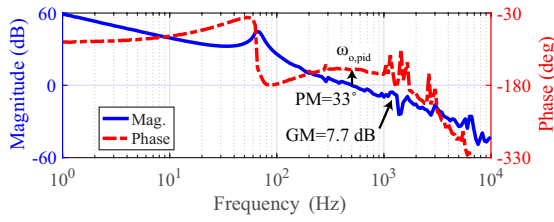
IEEE TRANSACTIONS ON INDUSTRIAL ELECTRONICS

Fig. 5. Simulated open-loop transfer function for the design of $C_{pid}(s)$, indicating the gain margin (GM) and the phase margin (PM).

B. Robust stability

Due to the thermal expansion and the nonlinearity of the flexures (Sec. V-E), the stiffness k may vary during AFM operation. Similarly, m_m may slightly vary when the AFM probe is exchanged. To investigate the influence of such parametric uncertainties, scale factors δ_m, δ_c, and δ_k are introduced for m_m, c, and k, respectively, and they are included in ζ as follows:

$$\zeta_\delta = \frac{\delta_c c}{2\sqrt{\delta_k k \delta_m m_m}} = \frac{\delta_c}{\sqrt{\delta_k \delta_m}}\zeta, \qquad (14)$$

In the same manner, g_p and ω_1 include the scale factors as follows:

$$g_{p,\delta} = g_p/\delta_k, \qquad \omega_{1,\delta} = \omega_1\sqrt{\delta_k/\delta_m}. \qquad (15)$$

The plant parameters with the scale factors are used to simulate the open-loop transfer function $P_{pl}(s)P(s)C_{pid}(s)$. In this simulation, δ_m is changed between 99 % and 101 % as a worst case because the weight of the exchangeable AFM probe and chip is only 0.2 % of m_m. Similarly, δ_k and δ_c are changed in a relatively large range between 50 % and 150 %.

Fig. 6(a)(b) shows the simulation results when δ_m, δ_c, and δ_k are individually and simultaneously changed. The variation of the dynamics are significant around ω_1 and below due to δ_k and δ_c. Nevertheless, the 33° PM is ensured with a sufficient GM for closed-loop stability. This is because of the wide frequency band between ω_1 and ω_2, where the plant dynamics with the -40 dB/dec line are approximated by

$$P_a(s) \approx P(s) \approx g_a K_m/(m_m s^2), \qquad (16)$$

which is insensitive to k and c. Due to the insensitivity and the small variation of δ_m, sufficient stability margin is ensured despite the parametric uncertainties. Note that the crossing of the phase over the -180° line between 40 Hz and 100 Hz in Fig. 6(a) is irrelevant to stability margin because the gain below 100 Hz is much higher than 0 dB. In fact, the corresponding locus below 100 Hz is far from the -1 point on the Nyquist diagram, without influencing GM and PM (Fig. 6(b)).

The controller realizes the high open-loop gain of more than 20 dB around ω_1 and below in Fig. 6(a). Consequently, the complementary sensitivity function $T_m(s)$ (the transfer function from r_m to z_m without $C_{ff}(s)$ in Fig. 3) shows a flat gain up to about 1 kHz even with the varied scale factors, as simulated in Fig. 7. In summary, robust stability is realized to compensate for the first resonance by widening the frequency
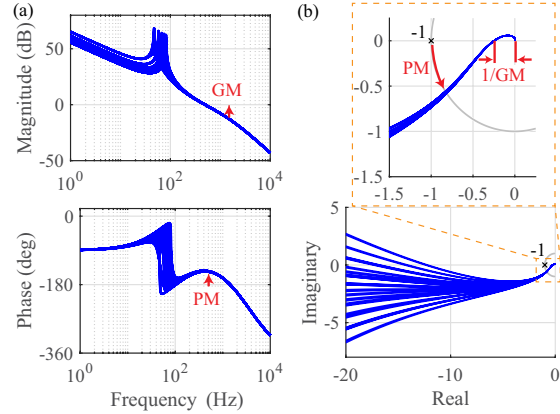

Fig. 6. Simulated open-loop transfer function $P_{pl}(s)P(s)C_{pid}(s)$ indicating PM and GM of 33° and 12 dB, respectively, where the scale factors δ_m, δ_c, and δ_k are included to change for robust stability analysis: (a) Bode plot and (b) Nyquist diagram.
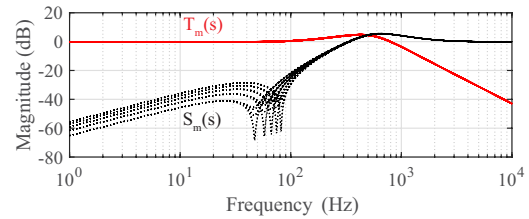

Fig. 7. Simulated complementary sensitivity function $T_m(s)$ and sensitivity function $S_m(s)$ of the position loop, where the scale factors δ_m, δ_c, and δ_k are included to vary.

band between ω_1 and ω_2 and by setting the open-loop crossover frequency $\omega_{o,pid}$ within the band.

C. Disturbance rejection

A problem of large-range AFMs in general is their suspension mode at a relatively low frequency, which can be excited by disturbances to impair the positioning resolution [37]. The disturbances include the noise of the current amplifier and the digital-to-analog converter, as well as floor vibrations. The resulting mover vibrations can be modeled as d_z in Fig. 3 and appear as artifacts in the topography image of conventional AFMs [37]. In the case of the proposed AFM, $C_{pid}(s)$ rejects d_z for high positioning resolution of the mover to improve the imaging quality.

While $C_{pid}(s)$ is inactive, the mover position z_m is equal to d_z. When $C_{pid}(s)$ is turned on with $r_m = 0$, z_m is given by

$$z_m(s) = d_z(s)(1 + P_a(s)C(s))^{-1} = d_z(s)S_m(s), \qquad (17)$$

where $S_m(s)$ is the sensitivity function of the position loop. Thus, $S_m(s)$ quantifies the improvement of the positioning resolution by turning on $C_{pid}(s)$. To analyze its effectiveness, $S_m(s)$ is simulated by including and changing the scale factors δ_m, δ_c, and δ_k in the same manner as Section V-B. The simulation results in Fig. 7 reveal that $C_{pid}(s)$ rejects d_z below

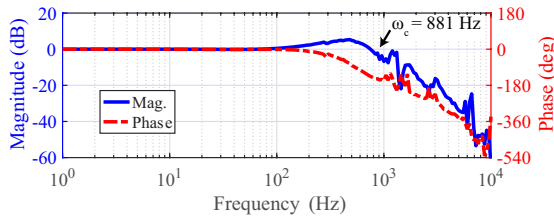IEEE TRANSACTIONS ON INDUSTRIAL ELECTRONICS

Fig. 8. Measured Bode plot of $G_m(s)$ from the mover position reference r_m to the measured position y_m, indicating the -3 dB control bandwidth ω_c of 881 Hz.

Fig. 9. Measured mover position y_m by using a 1 Hz sine wave with an amplitude of $\pm 350\,\mu m_{pp}$ as the mover position reference when the 2-DOF position control is turned off, when only the feedback controller $C_{pid}(s)$ is turned on, and when both $C_{pid}(s)$ and $C_{ff}(s)$ are active.

260 Hz even if the plant parameters vary. More importantly, $S_m(s)$ has notches because the first resonance increases the plant gain in (17). In other words, the proposed AFM utilizes the first resonance to effectively reject the disturbances. Due to the resulting steep slope around 100 Hz, more than 90 % of the vibrations can be rejected below 100 Hz for high positioning resolution of the mover.

D. Feedforward control

Due to the integrator of $C_{PID}(s)$, the resulting closed-loop Lorentz actuator is a Type 1 system and cannot track the reference motion when it is a ramp signal [36]. This is problematic, especially when the AFM sample is tilted because z_s contains a ramp signal in Fig. 3. As a solution, a feedforward controller $C_{ff}(s)$ is designed as follows:

$$C_{ff}(s) = P^{-1}(s)\left(\frac{s^2}{\omega_{lpf}^2} + \sqrt{2}\frac{s}{\omega_{lpf}} + 1\right)^{-1}, \qquad (18)$$

where ω_{lpf} is the cut-off frequency of the low-pass filter to make $C_{ff}(s)$ proper. It is set to 1 kHz because the modeling error of $P(s)$ increases above that frequency in Fig. 4.

E. Evaluation

To evaluate the achieved control bandwidth, the closed-loop transfer function from r_m to y_m, which is denoted by $G_m(s)$ in Fig. 3, is measured, as shown in Fig. 8. As indicated, the -3 dB control bandwidth ω_c is 881 Hz, which is 13.2 times higher than the first resonant frequency ω_1. This result clearly demonstrates that the proposed AFM overcomes the bandwidth limitation of the conventional AFMs, that is ω_1.

A concern of the leaf spring flexures is a nonlinear motion due to the symmetrical design without ancillary movers [26], [29]. Thus, a sine wave of 1 Hz is used as the mover position reference r_m to evaluate nonlinearity. Its amplitude is set to $700\,\mu m_{pp}$, the root mean square (rms) of which is close to $z_{max,dc}$. Fig. 9 shows the measured mover position. When the AFM is evaluated without control (open loop), the sine wave is scaled by g_p^{-1} as the reference. In Fig. 9, the reference-position trajectory is curving, which is quantified by the full scale nonlinearity of 5.4 %. By using the feedback controller $C_{pid}(s)$, the nonlinearity is significantly decreased to 0.051 %. The combination with $C_{ff}(s)$ further improves it to 0.020 % for higher accuracy. Fig. 9 additionally demonstrates a long
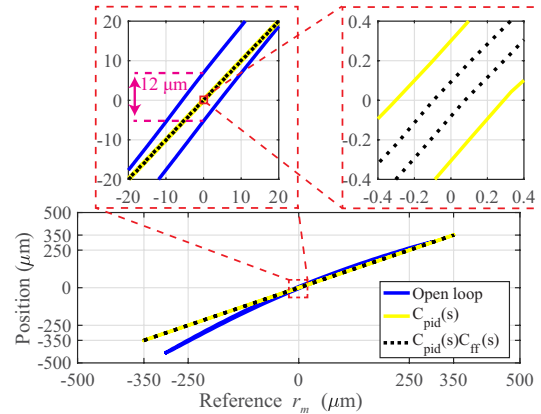
range motion of $700\,\mu m$, which is approximately 70 times larger than typical AFMs.

As indicated in the magnified plot (left) of Fig. 9, the width of the loop at $r_m = 0\,\mu m$ is $12\,\mu m$ for the $713\,\mu m$ motion without control. This is significantly smaller than the hysteresis loop of piezoelectric actuators, the hysteresis nonlinearity of which is typically up to 20 % [38]. The PID controller decreases the width of the loop to approximately $0.6\,\mu m$. This tracking error occurs due to the Type 1 system because the 1 Hz sine trajectory has a relatively uniform velocity around the origin, which is regarded as a ramp input. The feedforward controller $C_{ff}(s)$ successfully decreases the tracking error, as intended in Section V-D.

To evaluate the disturbance rejection and the positioning resolution, the mover position is measured when the 2-DOF position controller is turned off and on with $r_m = 0$, as shown in Fig. 10(left). Without control, the mover fluctuates more than ± 25 nm due to the disturbances. The rms error is 13.5 nm, which is the positioning resolution. The position controller reduces the fluctuation below ± 10 nm and improves the positioning resolution to 1.7 nm. The power spectral density (PSD) of the measured vibrations show that they are rejected below 260 Hz, verifying the discussions in Section V-C. Particularly the vibrations excited by the suspension mode around 60 Hz are trimmed since $C_{pid}(s)$ utilizes the mode for better rejection. While the residual vibrations around 20 Hz are caused by the floor vibrations, the peaks at 50 Hz, 100 Hz, and 150 Hz would be due to the 50 Hz main.

Notice that the flexures designed for high ω_2 exhibit nonlinearity but enable the high-bandwidth control. Consequently, the disturbances are well-rejected for the high positioning resolution. Furthermore, the high-bandwidth control provides a high open-loop gain (app. 60 dB at 1 Hz in Fig. 5), compensating for the flexure nonlinearity in return. In other words, the mechanism and the control are complementing each other well, resulting in the synergy as intended by DFC. This mechatronic system is fundamentally different from the flexure-guided
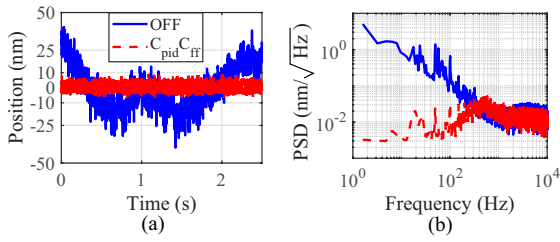
IEEE TRANSACTIONS ON INDUSTRIAL ELECTRONICS

Fig. 10. Measured mover position y_m (a) in the time domain and (b) its power spectral density (PSD) when the 2-DOF position control is turned off and on with the mover position reference $r_m = 0$ nm.

systems that achieve certain performance by the flexure design only [29], [39]. As a result of the well-integrated mechatronic system design, the vertical actuator successfully realizes the high resolution, the high accuracy, the large range, and the high bandwidth simultaneously. Specifically speaking, the product of the demonstrated motion range (700 μm) and the achieved control bandwidth (881 Hz) is equal to 617 kHz·μm. Therefore, the vertical probe motion of the proposed AFM breaks through the theoretical limit of 567 kHz·μm for the piezo-actuated systems in (1).

VI. DEFLECTION CONTROL

A. Controller tuning

To utilize the high-performance actuator for the AFM operation in the constant force mode, the probe deflection is controlled by a feedback controller. Although the sensitivity k_p of the probe with its preamplifier is nominally 0.3 mV/nm, it may vary, for example, when the probe is exchanged. Therefore, model-free control is applied by using an I controller k_i/s as $C_i(s)$ in Fig. 3. After the probe engages with a sample, the integral gain k_i is increased until the probe output y_p oscillates, and then the gain is decreased by approximately 40 % for closed-loop stability. This tuning procedure is carried out every time the probe engages with the sample.

B. Validation

The deflection control is evaluated in a closed loop by measuring the open-loop transfer function $C_i(s)G_m(s)$, the sensitivity $S_p(s)$ from the deflection reference r_p to the error e_p, and the complementary sensitivity function $T_p(s)$ from r_p to y_p (see Fig. 3). Fig. 11 shows the results. The gain of the open-loop transfer function crosses the 0 dB line multiple times, and the lowest PM of 56.5° is seen at 519 Hz. Similarly, its phase crosses the -180° line multiple times with the lowest GM of 4.3 dB at 708 Hz.

In Fig. 3, the sample position z_s is regarded as output disturbances to be rejected by $C_i(s)$. Due to its relevance to the disturbance rejection problem, $S_p(s)$ is used to determine the -3 dB control bandwidth, which is 197 Hz. This is three times higher than the first resonant frequency $\omega_1 = 66.7$ Hz. Overall, the validation confirms that the deflection control of the proposed AFM also overcomes the bandwidth limitation of the conventional AFMs, that is ω_1.
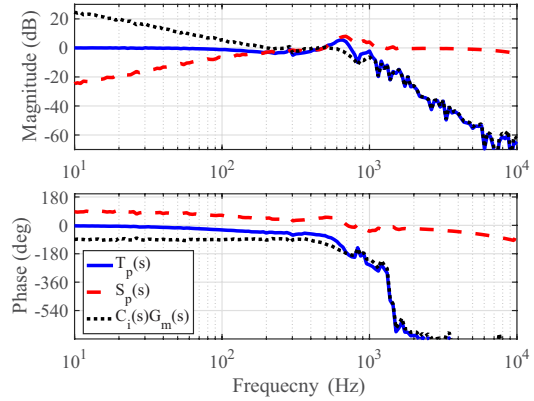

Fig. 11. Measured Bode plot with the deflection control: the open-loop transfer function $C_i(s)G_m(s)$, the sensitivity $S_p(s)$ from the deflection reference r_p to the error e_p, and the complementary sensitivity function $T_p(s)$ from r_p to y_p.

VII. AFM EXPERIMENTS

The limited workspace of typical AFMs poses miscellaneous problems. For example, an AFM sample under thermal testing cannot be continuously imaged because it expands or shrinks beyond the vertical motion range of the probe [40]. To demonstrate that the proposed AFM overcomes such problems, the sample is vertically moved $\pm 200 \mu$m by the manual Z stage while the AFM is active without XY scanning. The results are shown in Fig. 12, where the offset of the probe signal y_p is removed by tuning its preamplifier to indicate the deflection error. Even when the manual Z stage vertically moves the sample, the deflection control maintains y_p below ± 0.7 V. Consequently, the mover position reference r_m successfully captures the sample motion as the topography change of $\pm 200 \mu$m.

Fig. 12(c) magnifies r_m between 29 s and 30 s when the manual Z stage is stationary. The plot indicates that r_m fluctuates within a band of ± 10 nm with a standard deviation of 2.9 nm. It is the vertical resolution of the topography measurement and further discussed in Section VIII. In summary, the proposed AFM is capable of the long-range topography measurement with the 197 Hz bandwidth and the single nanometer resolution.

To further demonstrate the achieved vertical resolution, CD-ROM pits are imaged. The reflective film of a CD-ROM is removed to expose the polycarbonate surface that has pits with a width of about 500 nm and a height close to 120 nm [41], [42]. The XY scanner tracks a 2 Hz triangular signal and a ramp signal as the trajectory for raster scanning of the sample. This setting requires 100 s to record data for an image with 200 lines. Fig. 13 shows the resulting image. The CD-ROM pits are clearly resolved due to the single nanometer resolution of the AFM.

VIII. DISCUSSIONS

As evaluated in Section VII, the vertical resolution of the topography measurement is 2.9 nm. This is because r_m in-
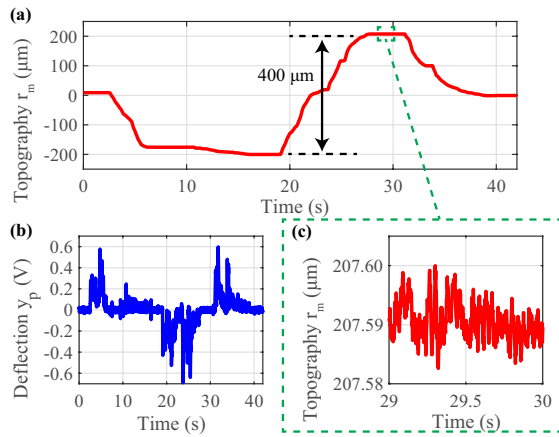
Fig. 12. Measured AFM probe's output y_p and mover position reference r_m for the high topography measurement when the sample is vertically moved 400 μm by the manual Z stage.
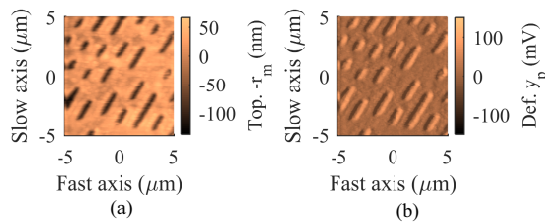

Fig. 13. Imaged CD-ROM pits: (a) topography and (b) deflection images.

cludes the probe's measurement noise, the floor vibrations, and the position sensor's measurement noise. Particularly floor vibrations are a common problem of AFMs with large samples and fully automated AFMs. These AFMs have a long mechanical loop between the probe and sample, and the loop rigidity is impaired [1], [37]. Consequently, they are sensitive to floor vibrations. This problem can be solved by integrating the sample-tracking vibration isolation [35]. A disadvantage of the proposed AFM in comparison with conventional AFMs is the measurement noise of the position sensor, which is modeled by n_m in Fig. 3. It is fed back by $C_{pid}(s)$ and included in r_m. Therefore, a position sensor with sufficiently low noise has to be selected when high imaging resolution is required. In return of the resolution influenced by the position sensor, the proposed AFM achieves excellent performance on the range, the bandwidth, the robustness, and the linearity.

For further discussion, the proposed AFM is compared with other flexure-guided AFMs in Table II, In this table, AFMs with piezoelectric vertical actuators are excluded since they are unsuitable for the required range of hundreds of micrometers, as discussed in the introduction. The problematic resonant frequency ω_{pr} that limits the achievable bandwidth is ω_1 in the case of conventional AFMs, and their range-frequency product $z_{max}\omega_{pr}$ in Table II is up to 100 kHz·μm, which is far smaller than the theoretical limit of piezoelectric actuators (567 kHz·μm). In the case of the proposed AFM, the

position control compensates for the first resonance, and ω_2 becomes ω_{pr}. Consequently, $z_{max}\omega_{pr}$ can be a significantly higher value of 805 kHz·μm. Furthermore, the position control enables the disturbance rejection and the robustness against the variation of ω_1, which cannot be usually realized by conventional AFMs.

Overall, the proposed AFM successfully demonstrates a long measurement range with a high measurement bandwidth of topography by using the long-range vertical actuator with a high control bandwidth, which is realized by fusing the flexure design and the control design.

IX. CONCLUSION

Design for control is applied to a flexure-guided Lorentz actuator that vertically moves an AFM probe. The second resonant frequency of the actuator is maximized for a high control bandwidth while the first resonant frequency is relatively low for a large motion range. This design ensures a large frequency band of more than a decade between the two resonances. Consequently, the dynamics within the band are dominated by the -40 dB/dec mass line. Due to the simple dynamics, a 2-DOF controller with a position sensor is able to realize a control bandwidth of 881 Hz that is 13.2 times higher than the first resonance, achieving a full-scale nonlinearity of 0.02 % for the 700 μm motion range with a resolution of 1.7 nm. The achieved range-bandwidth product of the actuator is 617 kHz·μm, breaking through a theoretical limit of piezo-actuated systems. Furthermore, the controller realizes high robustness against the variation of the first resonance and rejects disturbances for high positioning resolution. With the high-performance actuator, the deflection control is implemented for topography measurement, experimentally demonstrating a bandwidth of 197 Hz and a measurement range 400 μm. The vertical resolution of the measurement is 2.9 nm, and the AFM successfully generates a 3-D image of nanostructures.

REFERENCES

[1] P. Eaton and P. West, *Atomic Force Microscopy*. Oxford University Press, 2010.

[2] H. Xie, Y. Wen, X. Shen, H. Zhang, and L. Sun, "High-speed afm imaging of nanopositioning stages using h∞ and iterative learning control," *IEEE Transactions on Industrial Electronics*, vol. 67, DOI 10.1109/TIE.2019.2902792, no. 3, pp. 2430–2439, Mar. 2020.

[3] G. Binnig, C. F. Quate, and C. Gerber, "Atomic force microscope," *Phys. Rev. Lett.*, vol. 56, DOI 10.1103/PhysRevLett.56.930, pp. 930–933, Mar. 1986.

[4] M. Loganathan, A. Al-Ogaidi, and D. A. Bristow, "Design and control of a dual-probe atomic force microscope," *IEEE/ASME Transactions on Mechatronics*, vol. 23, DOI 10.1109/TMECH.2017.2779241, no. 1, pp. 424–433, Feb. 2018.

[5] A. Keyvani, M. S. Tamer, M. H. van Es, and H. Sadeghian, "Simultaneous AFM nano-patterning and imaging for photomask repair," in *Proc. SPIE 9778, Metrology, Inspection, and Process Control for Microlithography XXX*, vol. 9778, DOI 10.1117/12.2219041, 2016.

[6] T.-F. Yao, A. Duenner, and M. Cullinan, "In-line metrology of nanoscale features in semiconductor manufacturing systems," *Precision Engineering*, vol. 47, DOI 10.1016/j.precisioneng.2016.07.016, pp. 147 – 157, 2017.

ACIN

TABLE II
PERFORMANCE OF AFMs USING FLEXURE-GUIDED ACTUATORS THAT ARE NOT PIEZOELECTRIC FOR THE VERTICAL PROBE MOTION.

Ref.	Range z_{max}	Problematic Res. ω_{pr}	$z_{max}\omega_{pr}$ (kHz·μm)	Vertical Resolution	Linearity
[18]	140 μm	< 600 Hz	< 84	-	-
[19]	-	270 Hz	-	≈ 1 nm$_{pp}$	Good
[14]	> 1 mm	85 Hz	> 85	-	-
[43]	84 μm	257 Hz	22	55 nm$_{pp}$	-
[20]	225 nm	104 kHz	23	-	Good
This work	700 μm	1.15 kHz	805	2.9 nm$_{std}$	0.02 %

[7] R. Schmitt and F. Moenning, "Ensure success with inline-metrology," in *IMEKO XVIII World Congress*, 2006.

[8] H. A. Ching, D. Choudhury, M. J. Nine, and N. A. A. Osman, "Effects of surface coating on reducing friction and wear of orthopaedic implants," *Science and Technology of Advanced Materials*, vol. 15, DOI 10.1088/1468-6996/15/1/014402, p. 014402, 2014.

[9] S. Chen, C. Cheung, C. Zhao, and F. Zhang, "Simulated and measured surface roughness in high-speed grinding of silicon carbide wafers," *The International Journal of Advanced Manufacturing Technology*, vol. 91, DOI 10.1007/s00170-016-9805-8, no. 1, pp. 719–730, Jul. 2017.

[10] G. Schitter, K. J. Astrom, B. E. DeMartini, P. J. Thurner, K. L. Turner, and P. K. Hansma, "Design and modeling of a high-speed afm-scanner," *IEEE Transactions on Control Systems Technology*, vol. 15, DOI 10.1109/TCST.2007.902953, no. 5, pp. 906–915, Sep. 2007.

[11] T. Ando, "High-speed atomic force microscopy and its future prospects," *Biophysical Reviews*, vol. 10, DOI 10.1007/s12551-017-0356-5, no. 2, pp. 285–292, Apr. 2018.

[12] A. J. Fleming, "Nanopositioning system with force feedback for high-performance tracking and vibration control," *IEEE/ASME Transactions on Mechatronics*, vol. 15, DOI 10.1109/TMECH.2009.2028422, no. 3, pp. 433–447, Jun. 2010.

[13] R. Munnig Schmidt, G. Schitter, A. Rankers, and J. van Eijk, *The Design of High Performance Mechatronics*, 2nd ed. Delft University Press, 2014.

[14] H. Barnard, C. Randall, D. Bridges, and P. K. Hansma, "The long range voice coil atomic force microscope," *Review of Scientific Instruments*, vol. 83, DOI 10.1063/1.3683235, p. 023705, 2012.

[15] B. J. Kenton, "Design, characterization, and controlof a high-bandwidth serial-kinematic nanopositioning stagefor scanning probe microscopy applications," Master's thesis, University of Nevada, 2010.

[16] Y. K. Yong, S. O. R. Moheimani, B. J. Kenton, and K. K. Leang, "Invited review article: High-speed flexure-guided nanopositioning: Mechanical design and control issues," *Review of Scientific Instruments*, vol. 83, DOI 10.1063/1.4765048, p. 121101, 2012.

[17] P. Laugier and G. Haïat, *Introduction to the Physics of Ultrasound*, pp. 29–45. Springer Netherlands, 2011.

[18] T. Mariani, C. Frediani, and C. Ascoli, "A three-dimensional scanner for probe microscopy on the millimetre scale," *Applied Physics A*, vol. 66, DOI 10.1007/s003390051257, no. 1, pp. 861–866, Mar. 1998.

[19] W. Youm, J. Jung, S. Lee, and K. Park, "Control of voice coil motor nanoscanners for an atomic force microscopy system using a loop shaping technique," *Review of Scientific Instruments*, vol. 79, DOI 10.1063/1.2829990, no. 1, p. 013707, 2008.

[20] R. Sriramshankar and G. R. Jayanth, "An integrated magnetic actuation system for high-speed atomic force microscopy," *IEEE/ASME Transactions on Mechatronics*, vol. 23, DOI 10.1109/TMECH.2018.2857464, no. 5, pp. 2285–2294, Oct. 2018.

[21] G. Witvoet, J. Peters, S. Kuiper, S. Keyvani, and R. Willekers, "First results from the large dynamic range atomic force microscope for overlay metrology," in *Proc. SPIE 10959, Metrology, Inspection, and Process Control for Microlithography XXXIII*, vol. 10959, DOI 10.1117/12.2514044, 2019.

[22] A. Okyay, K. Erkorkmaz, and M. B. Khamesee, "Mechatronic design, actuator optimization, and control of a long stroke linear nano-positioner," *Precision Engineering*, vol. 52, DOI 10.1016/j.precisioneng.2018.01.007, pp. 308–322, 2018.

[23] M. Thier, R. Saathof, A. Sinn, R. Hainisch, and G. Schitter, "Six degree of freedom vibration isolation platform for in-line nano-metrology," *IFAC-PapersOnLine*, vol. 49, DOI 10.1016/j.ifacol.2016.10.534, no. 21,

pp. 149 – 156, 2016, 7th IFAC Symposium on Mechatronic Systems MECHATRONICS 2016.

[24] Q. Li, W. J. Zhang, and L. Chen, "Design for control-a concurrent engineering approach for mechatronic systems design," *IEEE/ASME Transactions on Mechatronics*, vol. 6, DOI 10.1109/3516.928731, no. 2, pp. 161–169, Jun. 2001.

[25] S. Ito, F. Cigarini, and G. Schitter, "Flux-controlled hybrid reluctance actuator for high-precision scanning motion," *IEEE Transactions on Industrial Electronics*, DOI 10.1109/TIE.2019.2952829, 2019.

[26] S. Ito and G. Schitter, "Atomic force microscopy capable of vibration isolation with low-stiffness z-axis actuation," *Ultramicroscopy*, vol. 186, DOI 10.1016/j.ultramic.2017.12.007, pp. 9 – 17, 2018.

[27] T. Yamaguchi, M. Hirata, and C. Pang, *High-Speed Precision Motion Control*. Taylor & Francis, 2011.

[28] M. Baranwal, R. S. Gorugantu, and S. M. Salapaka, "Robust atomic force microscopy using multiple sensors," *Review of Scientific Instruments*, vol. 87, DOI 10.1063/1.4960714, no. 8, p. 083704, 2016.

[29] H. Soemers, *Design Principles for Precision Mechanisms*. T-Pointprint, 2011.

[30] Q. Xu, "Design and development of a flexure-based dual-stage nanopositioning system with minimum interference behavior," *IEEE Transactions on Automation Science and Engineering*, vol. 9, DOI 10.1109/TASE.2012.2198918, no. 3, pp. 554–563, Jul. 2012.

[31] S. Ito, F. Cigarini, S. Unger, and G. Schitter, "Flexure design for precision positioning using low-stiffness actuators," *IFAC-PapersOnLine*, vol. 49, DOI 10.1016/j.ifacol.2016.10.548, no. 21, pp. 200 – 205, 2016, 7th IFAC Symposium on Mechatronic Systems MECHATRONICS 2016.

[32] F. Calignano, D. Manfredi, E. P. Ambrosio, S. Biamino, M. Lombardi, E. Atzeni, A. Salmi, P. Minetola, L. Iuliano, and P. Fino, "Overview on additive manufacturing technologies," *Proceedings of the IEEE*, vol. 105, DOI 10.1109/jproc.2016.2625098, no. 4, pp. 593–612, Apr. 2017.

[33] S. Farah, D. G. Anderson, and R. Langer, "Physical and mechanical properties of PLA, and their functions in widespread applications - a comprehensive review," *Advanced Drug Delivery Reviews*, vol. 107, DOI 10.1016/j.addr.2016.06.012, pp. 367–392, 2016.

[34] B. Tymrak, M. Kreiger, and J. M. Pearce, "Mechanical properties of components fabricated with open-source 3-D printers under realistic environmental conditions," *Materials & Design*, vol. 58, DOI 10.1016/j.matdes.2014.02.038, pp. 242–246, 2014.

[35] S. Ito, S. Unger, and G. Schitter, "Vibration isolator carrying atomic force microscope's head," *Mechatronics*, vol. 44, DOI 10.1016/j.mechatronics.2017.04.008, pp. 32 – 41, 2017.

[36] J. Van de Vegte, *Feedback Control Systems*, 3rd ed. Prentice Hall, 1994.

[37] J. H. Kindt, G. E. Fantner, J. A. Cutroni, and P. K. Hansma, "Rigid design of fast scanning probe microscopes using finite element analysis," *Ultramicroscopy*, vol. 100, DOI 10.1016/j.ultramic.2003.11.009, no. 3, pp. 259 – 265, 2004.

[38] K. A. Yi and R. J. Veillette, "A charge controller for linear operation of a piezoelectric stack actuator," *IEEE Transactions on Control Systems Technology*, vol. 13, DOI 10.1109/TCST.2005.847332, no. 4, pp. 517–526, Jul. 2005.

[39] H.-J. Lee, S. Woo, J. Park, J.-H. Jeong, M. Kim, J. Ryu, D.-G. Gweon, and Y.-M. Choi, "Compact compliant parallel xy nano-positioning stage with high dynamic performance, small crosstalk, and small yaw motion," *Microsystem Technologies*, vol. 24, DOI 10.1007/s00542-017-3626-z, no. 6, pp. 2653–2662, Jun. 2018.

[40] S. N. Nahar, "Phase-separation characteristics of bitumen and their relation to damage-healing," Ph.D. dissertation, Delft University of Technology, 2016.

[41] K. CLEMENTS, *Understanding and Servicing CD Players*. Newnes, 1994.

[42] F. Bruder and T. Fäcke, "Materials in optical data storage," *International Journal of Materials Research*, vol. 101, DOI 10.3139/146.110261, no. 2, pp. 199–215, 2010.

[43] S. Unger, S. Ito, D. Kohl, and G. Schitter, "Development of a compact atomic force microscope based on an optical pickup head," *IFAC-PapersOnLine*, vol. 49, DOI 10.1016/j.ifacol.2016.10.671, no. 21, pp. 629 – 635, 2016, 7th IFAC Symposium on Mechatronic Systems.

Shingo Ito received the MASc in Mechanical and Industrial Engineering from the University of Toronto, Canada, in 2007 and the PhD in Electrical Engineering from TU Wien, Vienna, Austria in 2015. From 2007 to 2010, he served as an engineer in the field of motion control at Yaskawa Electric Corporation, Japan.

He is currently a postdoctoral researcher at the Automation and Control Institute (ACIN), TU Wien. His research interest includes design and control of high-precision mechatronic systems for production, inspection, and automation, such as AFMs, laser scanners, and 3D printers.

Mathias Poik is PhD student in the group of Advanced Mechatronic Systems at the Automation and Control Institute (ACIN) at TU Wien, Austria. He received his MSc. in Energy Systems and Automation Technology from TU Wien in 2017.

His primary research interests are on precision engineering, focusing on Scanning Probe Microscopy and related measurement modes, as well as control of piezoelectric transducers.

Johannes Schlarp received the M.Sc. degree in electrical engineering from the Vienna University of Technology, Vienna, Austria, in 2017 and is currently working towards a Ph.D. degree in electrical engineering with the Automation and Control Institute, Vienna University of Technology, Vienna, Austria.

His primary research interests include high-performance mechatronic systems and precision engineering for automated in-line metrology.

Georg Schitter (SM'11) received the M.Sc. degree in electrical engineering from TU Graz, Austria in 2000, and the M.Sc. degree in information technology and the Ph.D. degree in technical sciences from ETH Zurich, Zurich, Switzerland, in 2004.

He is currently a Professor for Advanced Mechatronic Systems with the Automation and Control Institute, TU Wien, Vienna, Austria. His research interests include high-performance mechatronic systems, particularly for applications in the high-tech industry, scientific instrumentation, and mechatronic imaging systems, such as AFM, scanning laser and LIDAR systems, telescope systems, adaptive optics, and lithography systems for semiconductor industry.

Dr. Schitter received the IFAC Mechatronics best paper award (2008-2011) and 2013 IFAC Mechatronics Young Researcher Award, and was an Associate Editor for IFAC Mechatronics, Control Engineering Practice, and IEEE-TRANSACTIONS ON MECHATRONICS.